Scientia Iranica B (2017) 24(6), 2845–2855

Sharif University of Technology
Scientia Iranica
Transactions B: Mechanical Engineering
www.scientiairanica.com

Effect of Cu^{2+} ion on biological performance of nanostructured fluorapatite doped with copper

R. Nikonam Mofrad[a], S.K. Sadrnezhaad[b,*] and J. Vahdati Khaki[c]

a. *Department of Mechanical and Industrial Engineering, Concordia University, 1455 De Maisonneuve Blvd. W., Montreal, Quebec, Canada H3G 1M8.*
b. *Department of Materials Science and Engineering, Sharif University of Technology, Tehran, P.O. Box 11155-9466, Iran.*
c. *Department of Material Engineering, Faculty of Engineering, Ferdowsi University of Mashhad, Mashhad, P.O. Box 91775-1111, Iran.*

Received 8 June 2015; received in revised form 22 July 2016; accepted 7 January 2017

KEYWORDS
Nanostructured fluorapatite;
Ball milling;
Biological performance.

Abstract. Nanostructured copper-doped fluorapatite ($Cu_x.Ca_{(10-x)}.(PO_4)_6.F_2$) having crystallite sizes of 19, 29, and 34 nm at $x = 0.9$, 0.4, and 0.0, respectively, was synthesized by planetary ball milling of CaO, P_2O_5, CaF_2, and CuO powders. Specifications of the products were determined by Fourier-transform infrared spectroscopy, field emission scanning electron microscopy, transmission electron microscopy, and X-ray diffraction analyses. In-vitro studies and Mossman's Tetrazole Test (MTT) assays were also conducted by incubating $Cu_x.Ca_{(10-x)}.(PO_4)_6.F_2$ powder into Kokubo's Simulated Body Fluid (SBF) and against BT-20 cell, respectively, to determine bioactivity and biocompatibility of the materials. Antibacterial effects on Staphylococcus aureus were assessed by the disc diffusion test method. Measurements showed that the rate of formation of fluorapatite was lowered by Cu content. Besides, in-vitro experiments showed the same SBF interacted apatite precipitation for all samples. In contrast, MTT assays revealed different behavior for pure fluorapatite and apatite with $x = 0.9$ Cu against BT-20 cell after 24 h of incubation. This highlights the increase of fluorapatite cytotoxicity when Cu ion is present in the apatite structure. Copper-doped fluorapatite was, however, desirably antibacterial. This stemmed from copper ions interactions with the bacterial metabolism which resulted in enzymes neutralization and copper-doped fluorapatite antibacterial behavior.

1. Introduction

The well-known biocompatible Calcium Phosphate (CP) fluorapatite ($Ca_{10}(PO_4)_6F_2$) has obtained a wide reputation for its ample applications in clinical use [1]. However, infections associated with implanted surgical devices may cause significant problems, such as implant failure considered to be a common clinical complication [2]. Therefore, synthesis of the metal ion-substituted bioceramics with antimicrobial properties can be a good strategy to decrease the rate of biomaterials infections. Copper and its alloys have been registered in the U.S. Environmental Protection Agency (EPA) as the first solid antimicrobial material capable of deactivating microbes upon contact [3,4]. Copper-doped fluorapatite ($Cu_x.Ca_{(10-x)}.(PO_4)_6.F_2$), known as an effective, eco-friendly and heterogeneous catalyst in recent studies [5,6], is an interesting example of metal ion-substituted ceramic, which is to be discussed in this paper.

Among various methods of fluorapatite produc-

*. *Corresponding author. Tel.: +98 21 66165215; Fax: +98 21 66005717*
E-mail addresses: rahele_nikonam@ymail.com (R. Nikonam Mofrad); sadrnezh@sharif.edu (S.K. Sadrnezhaad); vahdati@um.ac.ir (J. Vahdati Khaki)

doi: 10.24200/sci.2017.4314

tion, the most common way of producing fine fluorapatite (FA) particles is mechanochemical synthesis method, which is considered as a subarea to Mechanical Alloying (MA) [7,8]. It has the advantages of simplicity, reproducibility, low cost, and ease of producing (even in bulk quantities) of nanostructured materials [9,10]. The outstanding biological potentials of nanostructured biomaterials, which have not been observed in the conventional polycrystalline coarse grained materials, have been reported by previous studies [11-13].

In this study, the effect of doping copper in nanostructured fluorapatite with substitution of Cu^{2+} for Ca^{2+} on biological performances of fluorapatite is discussed. To study the biological properties of the material, both in-vitro and in-vivo conditions were taken into account. In-vitro evaluation of the samples produced under simulated physiological conditions indicated the change of bioactivity due to the incorporation of copper into the fluorapatite. MTT assay was also used to determine biocompatibility of the samples. The human breast cancer BT-20 cell line was cultured and treated with prepared samples at various concentrations. The antibacterial activities of the apatite samples against the microorganism of Staphylococcus aureus (as an aerobic Gram-positive bacterium) were investigated via disc diffusion test.

2. Materials and methods

2.1. Powder preparation

The starting precursors included calcium oxide (CaO, BDH, catalog no. 11021-462, min. 95% purity), phosphorous oxide (P_2O_5, BDH, catalog no. 21411, min. 98.5% purity), calcium fluoride (CaF_2,MERCK,product no. 102840, precipitated pure, a mean particle size of about 100 μm), and copper oxide (CuO, MERCK, product no. 102671, $\geq$ 96% purity, particle size $\leq$ 160 μm). The planned degree of substitution of Ca^{2+} by Cu^{2+} in the general formula $Cu_x.Ca_{(10-x)}.(PO_4)_6.F_2$ was $x = 0$, 0.4, and 0.9 for which the product was designated as FA, 4CuFA, and 9CuFA, respectively. The overall reaction leading to the formation of the nanostructured copper-doped fluorapatite is as follows:

$$3P_2O_5(s) + (9-x)CaO(s) + xCuO(s) + CaF_2(s) \rightarrow Cu_x.Ca_{(10-x)}.(PO_4)_6.F_2(s). \quad (1)$$

Milling of the mixture was carried out at rotating speed of 260 rpm in a planetary ball mill using stainless still balls of 1 cm diameter and ball-to-powder ratio of 40:1. Synthesis consisted of three stages. First, appropriate amounts of CaO and CaF_2 were loaded into the vial and mechanically activated for 3 h. The milled powder was labeled CF3. Second, CF3 was mixed with P_2O_5 and milled for 3, 6, 12, 24, and 48 h. The products were labeled CF3P3, CF3P6, CF3P12, CF3$P_2$4, and CF3P48, respectively. Third, appropriate amounts of CuO and P_2O_5 were added to CF3 and milled long enough to form 4CuFA and 9CuFA. The detailed sequences of the procedure used are illustrated in the flowchart given in Figure 1, and the weight percent of the starting materials is presented in Table 1.

2.2. Characterization

X-Ray Diffraction (XRD) by Philips Analytical X-Ray B.V diffractometer with Ni-filtered Cu $k\alpha$ radiation was used for phase analysis, size determination, and cell parameter calculation. Diffraction patterns were taken in 2θ range of 10° to 60° at a step size of 0.02° with a generating voltage of 40 kV and an electric current of 40 mA. Identification of the apatite phase was achieved by comparing the diffraction pattern of the powders with JCPDS standard of card No: #02-1088

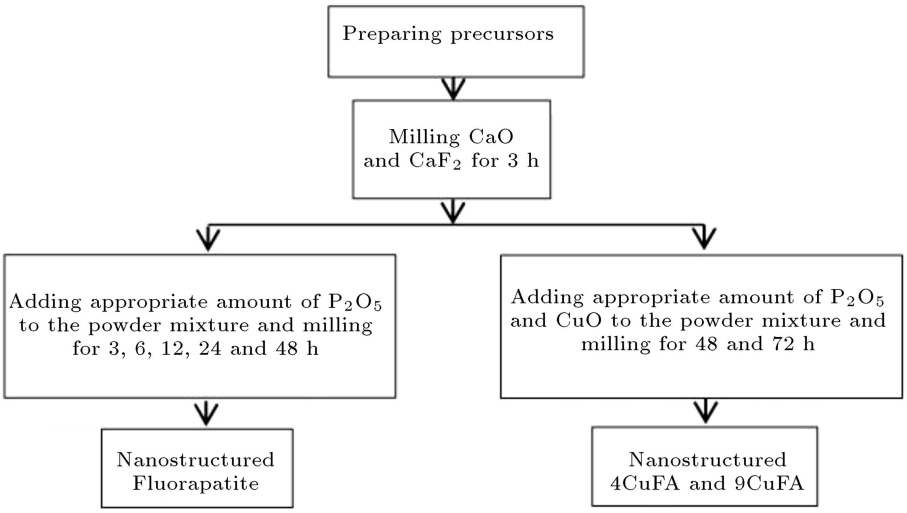

Figure 1. Flowchart indicating preparation procedure for FA, 4CuFA, and 9CuFA powders through mechanochemical route.

Table 1. Wt.% of the starting materials.

Product	Degree of substitution of Ca^{2+} by Cu^{2+}	Calculated chemical formula	Wt.% of the starting materials			
			P_2O_5	CaO	CuO	CaF_2
FA	$X = 0$	$Ca_{10}(PO_4)_6F_2$	42.21	50.04	0	7.74
4CuFA	$X = 0.4$	$Cu_{0.4}Ca_{9.6}(PO_4)_6F_2$	41.82	47.37	3.12	7.679
9CuFA	$X = 0.9$	$Cu_{0.9}.Ca_{9.1}(PO_4)_6F_2$	41.35	44.11	6.92	7.58

for CaO, #35-0816 for CaF_2, #85-1120 for P_2O_5, #74-1021 for CuO, #81-2040 for $Ca(OH)_2$, #85-0846 for $CaCO_3$, #83-0688 for H_3PO_4, #03-0604 for $Ca_2P_2O_7$ and #15-0876 for FA. The peak broadening of the XRD reflection was used to estimate the crystallite size of the powder based on Williamson-Hall formula (Eq. (2)) [14]:

$$\beta \cos\theta = 0.89(\lambda/d) + 4\varepsilon \sin\theta, \tag{2}$$

where d is crystallite size (nm), λ is wavelength of the X-rays, β is Full-Width at Half Maximum (FWHM) of each peak (rad), and θ is Bragg's diffraction angle (°). FWHM of (002), (222), and (213) reflections was taken to measure the crystallite sizes of the apatite powder.

Apatite lattice parameters (a and c) were calculated using the XRD data of (002) and (222) planes and the standard formula for the hexagonal (HCP) system (Eq. (3)) [15]:

$$\frac{1}{d^2} = \frac{4}{3}\left(\frac{h^2 + hk + k^2}{a^2}\right) + \frac{l^2}{c^2}, \tag{3}$$

where d is the spacing between adjacent planes in the set of Miller indices (hkl).

The functional groups of the powders were analyzed by using Fourier-transform infrared spectroscopy (FT-IR, ABB Bomen, MB 100) in the frequency range of 400-4000 cm^{-1} with the resolution of 4.0 cm^{-1} using KBr pellet technique.

Field emission scanning electron microscopy (FE-SEM, Hitachi, S-4160, Japan) operating at 15 kV was utilized to study the morphology and particle/agglomerate size distribution of the powders before and after soaking in the SBF solutions. Prior to this analysis, the as-prepared samples were coated with gold film using PVD method.

The powder morphology was studied via transmission electron microscopy analysis (TEM, LEO 912 AB, Germany) operated at an accelerating voltage of 120 kV. Before TEM observations, the samples were dispersed ultrasonically in ethanol and suspended on holey-carbon film-coated copper grids and allowed to air-dry.

Based on the results of Kokubo [16,17], the in-vitro bioactivity of materials can be investigated by the formation of bone-like apatite on the surface of the biomaterials in simulated body fluid. In order to evaluate the bioactivity of the prepared powders in the physiological conditions, we used, therefore, Kokubo's SBF and ion concentrations to be nearly equal to the human blood plasma, as shown in Table 2 [17]. The samples washed ultrasonically in acetone for 15 min were immersed into SBF and maintained there at 37.0°C for 14 days at a liquid/solid ratio of 1 ml/mg without refreshing the soaking medium. After the desired immersion time, the powders were filtered, gently washed with deionized water to remove the SBF, and dried at the room temperature. Variations in Ca^{+2} ions concentration and pH of SBF due to soaking of the apatite powders were measured by Inductivity Coupled Plasma-Optical Emission Spectroscopy (ICP-OES, Model OES-730, Varian), and pH meter. Morphology changes of the samples due to desolation and precipitation of bone-like apatite during the immersion were then determined by FE-SEM.

Biocompatibility of pure fluorapatite and fluorapatite with relatively high amount of Cu (9CuFA) on human breast cancer cell BT-20 was evaluated by MTT assay. The colorimetric assay based on the use of the tetrazolium salt MTT is relatively a rapid method for the quantitative measurement of surviving and proliferating cells. This method is based on the capacity of mitochondrial enzymes of viable cells to transform the yellow tetrazolium salt MTT into an insoluble, blue formazan product, which is measured spectrophotometrically. Since the reduction of MTT can only occur in metabolically active cells, the level of activity is a measure of the viability of the cells. The degree of the living cells can be measured through reading the results on a multi-well scanning

Table 2. Ionic concentrations of simulated body fluid [21].

Description	Ionic concentration (mM)							
	Na^+	K^+	Mg^{2+}	Ca^{2+}	Cl^-	HCO^{3-}	HPO_4^{2-}	SO_4^{2-}
Human plasma	142.0	5.0	1.5	2.5	103.0	27.0	1.0	0.5
SBF	142.0	5.0	1.5	2.5	147.8	4.2	1.0	0.5

spectrophotometer (ELISA reader) [18,19]. For this test, FA and 9CuFA concentrated elutes (not diluted) were prepared by adding culture medium supplemented with penicillin and streptomycin to FA and 9CuFA powder (1 mL to 100 mg of powder), according to the literature [20]. These elutes were then diluted by culture medium to the test concentrations (100%, 75%, 50%, 25%, 10%, 5%, and 1%) of FA and 9CuFA. Then, 200 μl cell suspension containing 10^4 cell was added to multi-well plate. After 24 h of incubation at 37°C, the medium was replaced with the fresh medium containing test concentration of elutes of FA and 9CuFA. Then, cells were exposed to the test concentration of elutes for 24 h. Four wells were used for each concentration. Blank control wells contained an appropriate volume of media, MTT and apatite powders without the presence of cells. Eight separate wells were filled with cells without the addition of elutes which acted as untreated control.

After the incubation time, 50% of media was removed, 10% V/V of MTT at 5 mg/ml was added to the remaining media to all wells of assay, and plates were further incubated at 37°C for 4 h. We carefully removed the medium and added (for 24-well plate) 500 μl DMSO to each well and mixed thoroughly to dissolve the dark blue crystals of formazan. We measured the absorbance by scanning multi-well spectrophotometer (ELAISA reader, BioTek model ELx800) using 570 nm test wavelength and 630 nm reference wavelength. The tests were performed on three replicate samples.

The percentage of cell survival rate was calculated using the following formula [19]:

$$\text{Survival rate } (\%) = \frac{At - Ab}{Ac - Ab} \times 100, \tag{4}$$

where At is average absorbance of the test compound, Ab is absorbance of blank, and Ac is average absorbance of the control material.

In order to evaluate the antibacterial effect of the samples, the disk diffusion method of Kirby and Bauer and the microorganism of Staphylococcus aureus (PTTC No. 1431) were used. About 0.085 g of each synthetic powder was pressed uniaxially to make discs of 6 mm diameter. The compressed disks were sterilized in an autoclave having temperature of 121°C for 20 min. Muller-Hinton Agar (MHA) was used as a growing nutrient medium for the microorganisms. MHA was cast into a plate. Tetracycline and Cloramphenicol was used as control material. The MHA containing plate was incubated with the test organism of 3×10^8 cells/ml. Three apatites and two antibiogram discs were placed on the surface of the agar. The plate was inverted and then placed in air incubator of 37°C for 20 h and 45 h. After these periods, the antimicrobial activities of the samples were examined by measuring zone of the inhibition of the bacterial growth around the discs. The results were then studied by Interpretative Chart of Zone Sizes as the standard guideline for the determination of the susceptibility level of microorganism to the antibiotics used [21] and to estimate the effect of copper ions on the bacterial metabolism.

3. Results and discussion

3.1. X-ray diffraction

The XRD pattern of the CaO-CaF_2 mixture, mechanically activated for 3 h (CF3), is shown in Figure 2(a). In this pattern, in addition to peaks attributed to CaF_2, some sharp peaks, assigned to calcium hydroxide ($Ca(OH)_2$), can also be detected. Since calcium oxide is unstable, a majority of calcium oxides were transformed into calcium hydroxide upon ambient water vapor adsorption. On the other hand, the presence of peak, which was assigned to calcium carbonate ($CaCO_3$), shows that amount of CaO was transformed to $CaCO_3$ during the milling process or originated from the starting CaO.

XRD patterns of CaO-CaF_2-P_2O_5 powder mixture (CF3P) milled for various durations are shown in

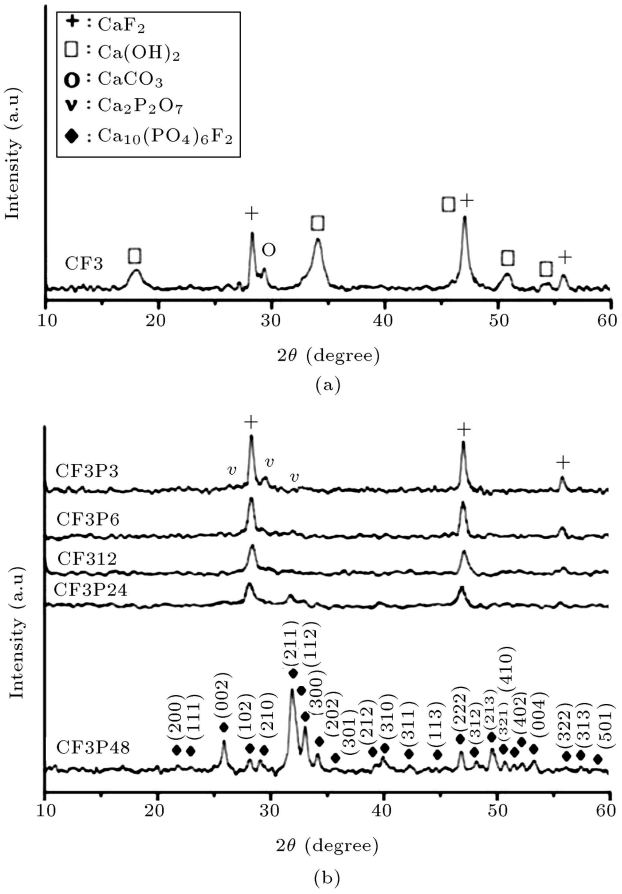

Figure 2. XRD pattern of the mechanically treated mixture of (a) CaO-CaF_2 and (b) CaO-CaF_2-P_2O_5.

Figure 2(b). As seen in the figure, sharp characteristic peaks of CaF_2 are present in the X-ray diffraction pattern of the 3 h milled samples (CF3P3). This pattern shows one peak at $2\theta = 29°$ which can correspond to $CaCO_3$. This peak can also be attributed to calcium phosphate ($Ca_2P_2O_7$) while the formation of this intermediate product is expectable when P_2O_5 is present. When mechanical activation extends to 12 h (CF3P12), this peak disappears and those corresponding to CaF_2 broaden. This confirms the continuation of the mechanochemical process. By rising the milling time up to 24 h (CF3P24), both broad and weak peaks around 31.8° emerge. This indicates the formation of poorly crystallized apatite phase. As milling time increased up to 48 h (CF3P48), a further increase in crystalline order of the apatite phase and further sharpening of the principal diffraction peaks occurred. Based on the XRD pattern, after 48 h milling, no peaks, except those assigned to FA, can be observed, which shows crystalline apatite phase achievement.

Figure 3 plots the XRD patterns of the FA powders doped with different amounts of copper. All peaks of the patterns correspond to the FA structure (JCPDS file card #15-0876). Only apatite phases are detected in the powder. This shows the complete reaction between precursors and suggests the formation of relatively well crystalline fluorapatite for all three samples during milling operations. Based on Figure 3, relatively well crystalline fluorapatite is synthesized after 48 h milling 4CuFA, while at higher Cu content (9CuFA), 72 h milling is required. Besides, this figure shows that with higher Cu content in the FA structure, less intensive apatite peaks form. Since the ionic radius of Ca^{2+} (0.99 Å) is larger than that of Cu^{2+} (0.72 Å), substitution of Cu^{2+} into Ca^{2+} position distorts the FA structure. The result shows the decrease of stability of the FA structure and subsequent lowering of the height of the apatite peaks [22].

The XRD patterns of the 9CuFA sample milled

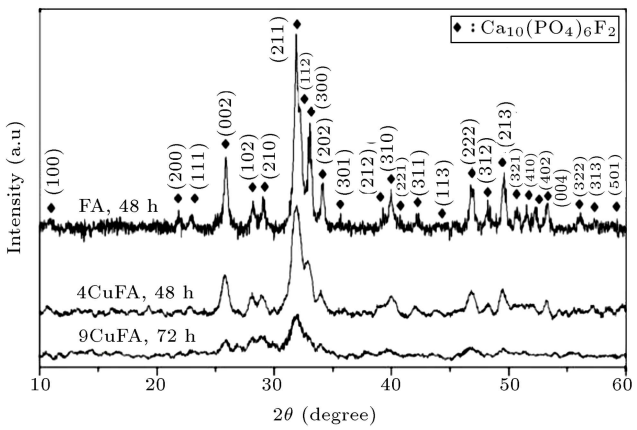

Figure 3. XRD patterns of synthesized FA, 4CuFA, and 9CuFA powders.

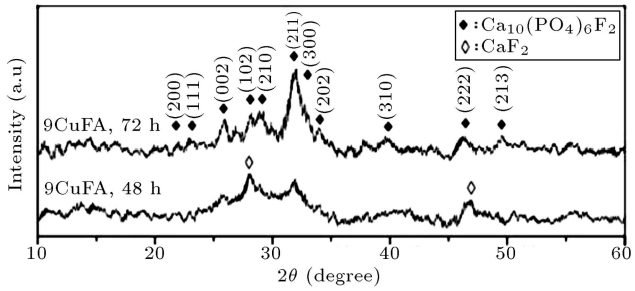

Figure 4. XRD patterns of mechanically treated mixture of CaO-CaF_2-P_2O_5-CuO ($x = 0.9$) after milling for various durations.

for 48 h and 72 h are shown in Figure 4. Two identified phases, including poorly crystallized apatite and CaF_2, are observed in the XRD patterns of the powder milled for 48 h. This is due to the incomplete reaction between the precursors. Prolonged milling up to 72 h causes an increase in crystalline order of the apatite phase, while the corresponding CaF_2 peaks completely disappear. Based on these observations, the relatively well-crystalline 9CuFA is synthesized after milling for 72 h. As a result, upon the addition of copper oxide to the powder mixture, CuO plays as an obstacle between the reactants to slow down the reaction at higher Cu content.

From XRD data and Williamson-Hall formula, the average crystallite size of FA and 4CuFA (after 48 h milling) and 9CuFA (after 72 h milling) are calculated to be 34, 29, and 19 nm, respectively. Measurements of the lattice parameters of the apatite powders indicate: $a = 0.9385$ nm and $c = 0.6870$ nm for FA, $a = 0.9366$ nm and $c = 0.6866$ nm for 4CuFA, and $a = 0.9361$ nm and $c = 0.6847$ nm for 9CuFA. The observed decreasing sizes of a and c parameters by increasing copper contents in the apatite structure refer to the substitution of Ca^{2+} by Cu^{2+}. Since the ionic radius of Cu is lower than Ca, incorporation of more Cu into the FA structure lowers the lattice parameters slightly. However, these values are close to the lattice parameters of the standard FA powder.

3.2. FTIR

Figure 5 records the IR spectra of FA powders with different copper concentrations. The FT-IR spectra for all of the three synthesized powders indicate nearly the same characteristic peaks for OH^-, PO_4^{3-}, and F...OH groups. These spectra show the existence of phosphate groups (PO_4^{3-}) at 471 cm^{-1} corresponding to asymmetrical υ_2 stretching vibration [23,24]. Besides, a doublet appears at 568 and 599 cm^{-1} corresponding to υ_4 bending vibrations [25,26]. As stated in the literature [27], the presence of the band at 743 cm^{-1} is due to the increase of F^- content in the (OH^-, F^-) apatite chain, while the configuration of OH...F is predominant in F^- rich chains containing only a few

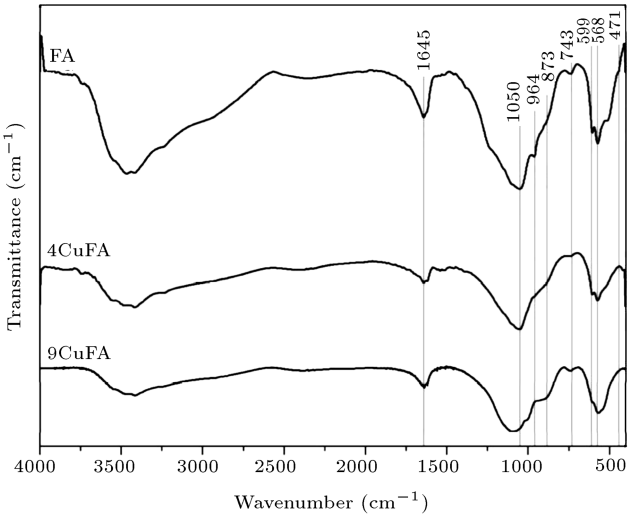

Figure 5. The IR spectra of the synthesized powders: (a) FA, (b) 4CuFA, and (c) 9CuFA.

(OH^-) and almost pure fluorapatite obtained. The band at 964 cm^{-1} relates to υ_1 bending vibrations of the phosphate group [25], while the most intense band in the spectra at 1050 cm^{-1} corresponds to asymmetrical υ_3 stretching vibration of the phosphate group [23,25]. According to this graph, substitution of Cu ion with shorter ionic radius than Ca brings about an increase in the P-O bonding strength [28], which shifts υ_1 and υ_3 vibrations to the higher frequencies. The presence of a peak at 873 cm^{-1} can be related to υ_2 stretching vibrations of the carbonate group which suggests substitution of CO_3^{2-} groups into PO_4^{3-} sites of apatite lattice (B-type substitution) [29]. By increasing the milling time from 48 h to 72 h, the amount of adsorbed carbonate group increases which enhances the intensity of the assigned peak at 873 cm^{-1}. Based on the fact that carbonates are constituents of hard tissue structures, the presence of low content of CO_3^{2-} groups in PO_4^{3-} sites could be beneficial to improve the bioactivity of FA and make it more similar to biological appetites [15]. The sharp band at 1645 cm^{-1} and the broad band over 3800-2500 cm^{-1} are mainly originated from the vibrations of the hydroxyl (OH^{-1}) group attributed to the presence of the absorbed water in the samples or the KBr pellet [23,24].

3.3. FE-SEM and TEM observations

Figure 6 shows microstructure and morphology of nanopowders after 48 h milling. From FE-SEM micrographs, it is revealed that both samples are composed of agglomerates/particles of irregular shapes with wide size distributions. No significant change in size distribution and morphology of the agglomerates/particles of samples can be inferred from these pictures. Also, higher magnifications show that the surface of particles is rather smooth before immersion. TEM micrographs of nanopowders after milling are shown in Figure 7. As illustrated, agglomerated particles are composed of smaller nanoparticles averaging from 20 to 60 nm mean diameter for FA and 4CuFa and 15 nm for 9CuFA. Prolonged milling of the latest sample results in the formation of fine particles, which are uniform in size and shape. Unlike 9CuFA, FA and 4CuFA are composed of relatively larger and irregular particles;

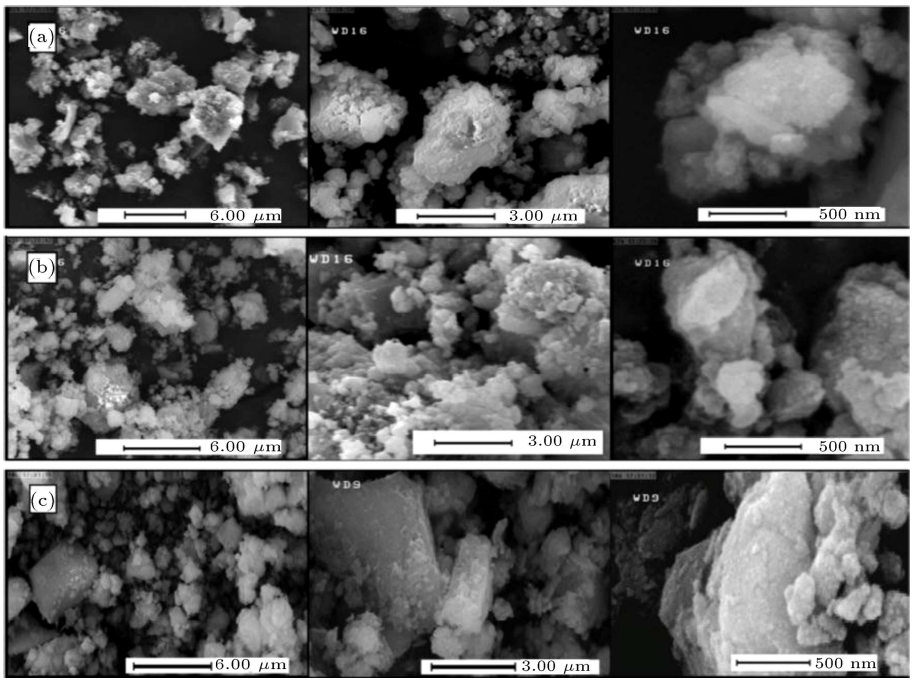

Figure 6. FE-SEM micrographs of (a) FA, (b) 4CuFA, and (c) 9CuFA powders at different magnifications.

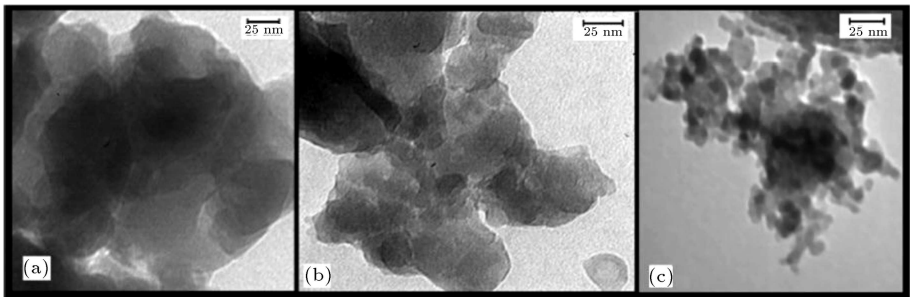

Figure 7. TEM images of (a) FA, (b) 4CuFA, and (c) 9CuFA powders at different magnifications.

however, both are similar in shape and morphology, typically semicircular crystals. These figures are in agreement with the crystallite sizes measured by XRD patterns through Williamson Hall equations.

3.4. In-vitro test

Variations of $[Ca^{2+}]$ and pH of SBF solutions as a function of soaking time are shown in Figures 8 and 9, respectively. Figure 8 indicates that the calcium ions concentration of SBF decreases as the incubation time increases. Besides, based on Figure 9, during this period,

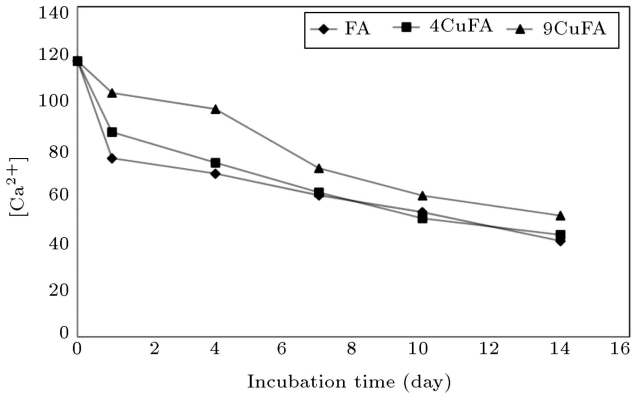

Figure 8. $[Ca^{+2}]$ profile of SBF solution containing prepared powders during the soaking time.

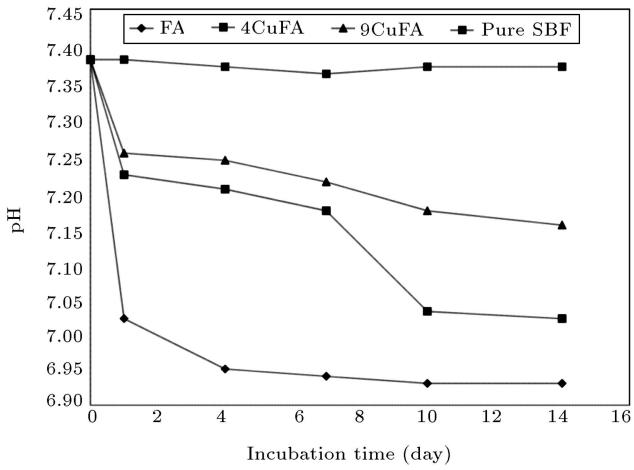

Figure 9. pH profile of SBF solution containing prepared powders during the soaking time.

the pH of pure SBF is relatively constant, whereas, in the case of 9CuFA, 4CuFA, and FA, the pH curves show a sudden drop during the first day. After that period, the pH values decrease slightly throughout the incubation time while reaching a minimum at the 14th day.

The observed trend of $[Ca^{2+}]$ and pH can be justified by the Kim's theory [30], which reveals that the process of bone-like apatite formation on the surface of biomaterials in the SBF is divided into the following stages. First, dissolution of apatite powder occurs, resulting in an increase in $[Ca^{2+}]$ and pH of SBF and appearance of negative charge on the surface of apatite particles. In the second step, the negative surface charge attracts Ca^{2+} ions to form the Ca-rich Amorphous Calcium Phosphate (ACP) layer. The resultant positive surface charge attracts the negative phosphate ion in the fluid to form Ca-poor ACP layers. $[Ca^{2+}]$ and pH of SBF decrease during this step. Finally, this layer gradually stabilizes and crystalizes into bone-like apatite in SBF. Indeed, when samples are immersed in SBF, simultaneous dissolution of the apatite particles and precipitation of the new apatite layer both occur. When precipitation is dominant, new apatite layers were formed, and tiny sediments precipitate on the surface of the immersed samples [31]. However, in this research, since no pH and $[Ca^{2+}]$ data are collected during the first hours of incubation, the first steps of dissolution behavior are not observed. The observed decrease in pH value and quantity of calcium ions of the SBF solution is due to the consumption of Ca^{2+} and OH^{-} ions during the second stage of the described theory and the formation of apatite layer.

Based on Figures 8 and 9, pH and $[Ca^{2+}]$ profiles of SBF solutions have relatively different decreasing rates. It can be seen that the reduction rate of pH and $[Ca^{2+}]$ profiles of sample decreases as the copper content increases. However, the concentrations of Ca^{2+} are relatively close in the case of FA and 4CuFA. As pointed out earlier, the replacement of Ca^{2+} by Cu^{2+} in FA causes a certain degree of disorder to the crystal structure which makes the lattice more unstable. Besides, with increasing of Cu content, the average grain size of FA slightly decreases which causes an increase in the volume of the grain boundaries. Therefore, by incorporation of Cu into the apatite structure, Gibbs

free energy increases and this may result in more solubility of 9CuFA apatite in SBF than FA. The observed higher amount of $[Ca^{+2}]$ in SBF for 9CuFA may be due to the dissolution behavior of 9CuFA during the first incubation hours and more calcium ion distribution. Therefore, higher value of pH in the case of 9CuFA than FA can be attributed to the higher amount of calcium ion in SBF solution for 9CuFA. However, a recent study has indicated that during incubation of FA powder in the SBF, concentration of different ions changes with time, which causes variation in the pH value of SBF. This happens due to the interaction between bioactive FA particles and the SBF solution which leads to the nucleation and growth of an apatite-like layer on the FA particles [23]. To interpret the observed behavior of the pH variations, other ions' concentrations should be considered in future studies.

In comparison with the samples before soaking in SBF (Figure 6), the microstructures of the particles soaked for 14 days (Figure 10) show the differences in their surface morphology. It is obvious from these micrographs that an interaction between the powders and SBF has occurred, a new bone-like apatite layer has been formed, and tiny sediments have precipitated on the surface of the immersed samples.

3.5. Cellular response on apatite samples

Figure 11 illustrates the MTT results of 24 h incubation of breast cancer cell in contact with FA and 9FA test concentrations. It is seen that by increasing the FA concentration, the proliferation response reaches a maximum at 25% FA. However, above 25% concentration, the viability decreases, yet it remains above the starting cell quantity. For higher concentrations, cell viability decreases steadily until it reaches the lowest at 100%. The observed cytotoxicity of FA at high concentrations is due to the presence of fluoride in the structure of FA [20]; however, it is worth mentioning that fluoride has high biological activity and wide biomedical applications to stimulate bone formation. For 9CuFA, for all concentrations, the viability percentage is lower than the control sample, which reveals that the presence of Cu ions in the apatite structure results in an increase of the cytotoxicity effect

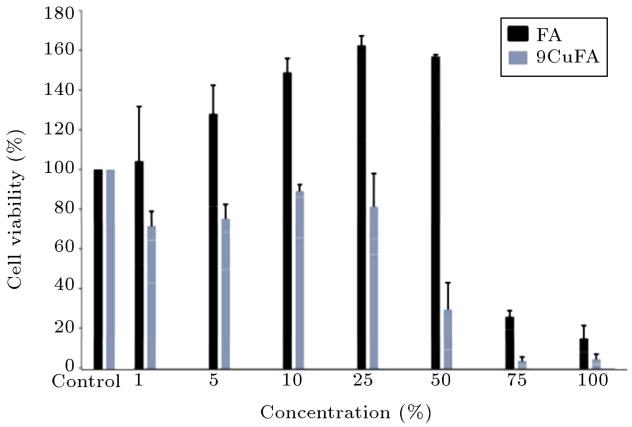

Figure 11. Viability of BT-20 cell in contact with apatite powders as a result of three individual experiments, while being compared with control wells containing only cell and media.

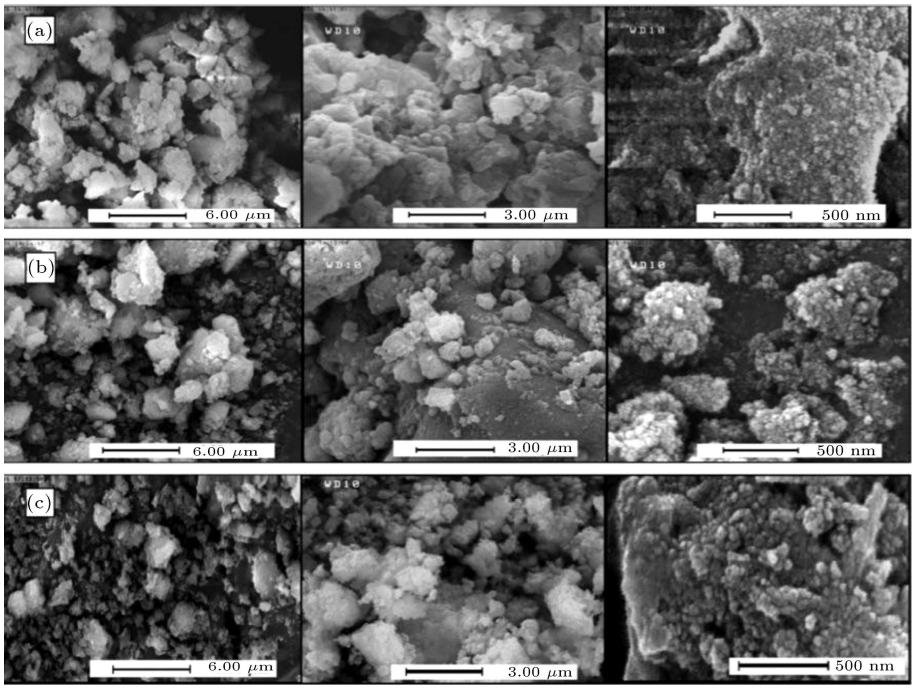

Figure 10. FE-SEM photographs of (a) FA, (b) 4CuFA, and (c) 9CuFA powders at different magnifications after soaking in SBF.

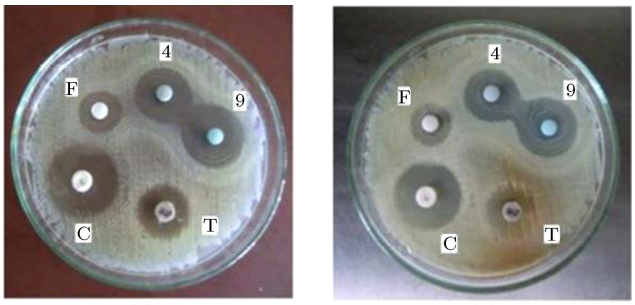

(a) (b)

Figure 12. Results of disc diffusion test of the synthetized samples after (a) 20 h and (b) 45 h of incubation. Definitions of characters on the plates are: F = pure FA, 4 = 0.4CuFA, 9 = 0.9CuFA, T = Tetracycline antibiogram and C = Cloramphenicolantibiogram.

of fluorapatite against BT-20 cell line. However, at 10% CuFA, the cell viability tends to the maximum of around 95% of the control sample, which is the lowest cytotoxicity achievable.

3.6. Antibacterial assessment

Results of antibacterial tests are presented in Figure 12. Both control disks and apatite samples of different copper contents clearly show the zones of inhibition. Recent studies have shown that fluoride can affect bacterial metabolism (as an enzyme inhibitor) and act as an antibacterial agent [32,33]. This leads to the presence of the zone of inhabitation around the pure FA disk. On the other hand, with an increase of the dose of the copper ions in the apatite structure, a growth in the zone of inhabitation is observed. This shows antibacterial activity improvement. With regard to the antibiotics used and the results derived from the Interpretative Chart of Zone Sizes [21], FA sample shows strong antibacterial property after doping with copper ions, which shows the complete inhibition of the growth of S.aureus bacteria. Indeed, Cu^{2+} ions react with bacteria and deactivate the S.aureus metabolism, thus inhibiting its growth even after 45 h of incubation. The mechanism of antibacterial activity of copper ions is as follows: Cu ions eluted from the material's surface are absorbed onto the surface of bacteria cells. These ions damage the cell membrane and penetrate into the bacteria. Cu-ions that have the strong reduction can extract the electrons from the bacteria, causing their cytoplasm to run off and oxidizing their cell nucleus and killing them [34,35].

We should consider that cell responses of biomaterials are various against different cultured cells. For instance, fluoride has shown considerably higher cytotoxicity against tumor cell lines than normal cells [36]. Besides, in this study, just high concentration of the prepared samples is investigated which may result in different observation than concentrations lower than 1% of sample test. Considering that biomaterials may have different potential risks to human safety, they can be utilized for various applications with respect to the extent of contact with patient's tissue. Therefore, to determine the exact biological response of copper ions on apatite structure, more exhaustive and comprehensive studies are required.

4. Conclusions

Nanostructured copper doped fluorapatites of different copper contents were synthesized using CaO, CaF_2, P_2O_5, and CuO as the starting materials through mechanochemical route. The results of Williamson-Hall equation and TEM analysis showed that the synthetic FA powders were not only nano-structured, but consisted of nano-particles, too. XRD results demonstrated that relatively pure FA and copper doped fluorapatite with the substitution ratio of 0.4 could be synthesized after milling for 48 h. Their respective crystallite sizes were 34 and 29 nm. The synthesis time mounted to 72 h, when the substitution ratio of copper doped fluorapatite was 0.9 and crystallite size became 19 nm. SEM micrographs along with in-vitro analysis showed the sedimentation of apatite-like tiny particles on the surface of all three samples. In-vitro test revealed that cell viability significantly increased following the treatment of BT-20 cell with FA from 1% to the high concentration of 50% and reached the max proliferation response at 25%. However, for 9CuFA, the presence of Cu ions showed signs of toxicity, especially at higher concentration than 25%. While high antibacterial activities were discerned for all three samples containing different amounts of copper, a positive correlation between copper content and the antibacterial properties was indicated.

Acknowledgment

The authors would like to appreciate the overall support of the research deputy of the Sharif University of Technology and Iran National Science Foundation (INSF).

References

1. Leroy, N., Bres, E., Jones, D. and Downes, S. "Structure and substitutions in fluorapatite", *Eur. Cell Mater.*, **2**, pp. 36-48 (2001).
2. Wan, Y., Xiong, G., Liang, H., Raman, S., He, F. and Huang, Y. "Modification of medical metals by ion implantation of copper", *Appl. Surf. Sci.*, **253**(24), pp. 9426-9429 (2007).
3. Ibrahim, M., Wang, F., Lou, M.M., Xie, G.L., Li, B., Bo, Z., Zhang, G.Q., Liu, H. and Wareth, A. "Copper as an antibacterial agent for human pathogenic multidrug resistant burkholderia cepacia

complex bacteria", *Journal of Bioscience and Bioengineering*, **112**(6), pp. 570-576 (2011).

4. Molteni, C., Abicht, H.K. and Solioz, M. "Killing of bacteria by copper surfaces involves dissolved copper", *Appl. Environ. Microbiol.*, **76**(12), pp. 4099-4101 (2010).
5. Mulla, S.A., Inamdar, S.M., Pathan, M.Y. and Chavan, S.S. "Ligand free, highly efficient synthesis of diaryl ether over copper fluorapatite as heterogeneous reusable catalyst", *Tetrahedron Lett.*, **53**(14), pp. 1826-1829 (2012).
6. Kantam, M.L., Venkanna, G., Kumar, K., Balasubrahmanyam, V., Venkateswarlu, G. and Sreedhar, B. "Mild and efficient alkylation of aldehydes by using copper fluorapatite as catalyst", *Advanced Synthesis & Catalysis*, **350**(10), pp. 1497-1502 (2008).
7. Suryanarayana, C. "Mechanical alloying and milling", *Progress in Materials Science*, **46**(1), pp. 1-184 (2001).
8. Aminzare, M., Eskandari, A., Baroonian, M.H., Berenovc, A., Razavi Hesabib, Z., Taheri, M. and Sadrnezhaad, S.K. "Hydroxyapatite nanocomposites: Synthesis, sintering and mechanical properties", *Ceramics International*, **39**(3), pp. 2197-2206 (2013).
9. Rhee, S. "Synthesis of hydroxyapatite via mechanochemical treatment", *Biomaterials*, **23**(4), pp. 1147-1152 (2002).
10. Eskandari, A., Aminzare, M., Hassani, H., Barounian, H., Hesaraki, S. and Sadrnezhaad, S.K. "Densification behavior and mechanical properties of biomimetic apatite nano-crystals", *Current Nanoscience*, **7**(5), pp. 776-780 (2011).
11. Shi, Z., Huang, X., Cai, Y., Tang, R. and Yang, D. "Size effect of hydroxyapatite nanoparticles on proliferation and apoptosis of osteoblast-like cells", *Acta Biomaterialia*, **5**(1), pp. 338-345 (2009).
12. Prabakaran, K. and Rajeswari, S. "Spectroscopic investigations on the synthesis of nano-hydroxyapatite from calcined eggshell by hydrothermal method using cationic surfactant as template", *Spectrochimica Acta Part A: Molecular and Biomolecular Spectroscopy*, **74**(5), pp. 1127-1134 (2009).
13. Torabi, M. and Sadrnezhaad, S.K. "Corrosion behavior of polypyrrole/hydroxyapatite nanocomposite thin films electropolymerized on NiTi substrates in simulated body fluid", *Materials and Corrosion*, **62**(3), pp. 252-257 (2011).
14. Williamson, G. and Hall, W. "X-ray line broadening from filed aluminum and wolfram", *Acta Metallurgica*, **1**(1), pp. 22-31 (1953).
15. Ebrahimi-Kahrizsangi, R., Nasiri-Tabrizi, B. and Chami, A. "Characterization of single-crystal fluorapatite nanoparticles synthesized via mechanochemical method", *Particuology*, **9**(5), pp. 537-544 (2011).
16. Kokubo, T. and Takadama, H. "How useful is SBF in predicting in vivo bone bioactivity?", *Biomaterials*, **27**(15), pp. 2907-2915 (2006).
17. Kokubo, T. "Bioactive glass ceramics: Properties and applications", *Biomaterials*, **12**(2), pp. 155-163 (1991).
18. Zarrabi, A., Shokrgozar, M.A., Vossoughi, M. and Farokhi, M. "In vitro biocompatibility evaluations of hyperbranched polyglycerol hybrid nanostructure as a candidate for nanomedicine applications", *J. Mater. Sci. Mater. Med.*, **25**(2), pp. 499-506 (2014).
19. Patel, S., Gheewala, N., Suthar, A. and Shah, A. "In-vitro cytotoxicity activity of solanum nigrum extract against hela cell line and vero cell line", *International Journal of Pharmacy and Pharmaceutical Sciences*, **1**(1), pp. 38-46 (2009).
20. Jantová, S., Theiszová, M., Letašiová, S., Birošová, L. and Palou, T. "In vitro effects of fluor-hydroxyapatite, fluorapatite and hydroxyapatite on colony formation, DNA damage and mutagenicity", *Mutation Research/Genetic Toxicology and Environmental Mutagenesis*, **652**(2), pp. 139-144 (2008).
21. Vandepitte, J., Verhaegen, J., Engbaek, K., Rohner, P., Piot, P. and Heuck, C. "Basic laboratory procedures in clinical bacteriology", *World Health Organization* (2003).
22. Li, M., Xiao, X., Liu, R., Chen, C. and Huang, L. "Structural characterization of zinc-substituted hydroxyapatite prepared by hydrothermal method", *Journal of Materials Science: Materials in Medicine*, **19**(2), pp. 797-803 (2008).
23. Fathi, M. and Mohammadi Zahrani, E. "Mechanical alloying synthesis and bioactivity evaluation of nanocrystalline fluoridated hydroxyapatite", *J. Cryst. Growth*, **311**(5), pp. 1392-1403 (2009).
24. Nikčević, I., Jokanović, V., Mitrić, M., Nedić, Z., Makovec, D. and Uskoković, D. "Mechanochemical synthesis of nanostructured fluorapatite/fluorhydroxyapatite and carbonated fluorapatite/fluorhydroxyapatite", *Journal of Solid State Chemistry*, **177**(7), pp. 2565-2574 (2004).
25. Nasiri-Tabrizi, B. and Fahami, A. "Synthesis and characterization of fluorapatite-zirconia composite nanopowders", *Ceram. Int.*, **39**(4), pp. 4329-4337 (2013).
26. Albano, M.P. and Garrido, L.B. "Processing of concentrated aqueous fluorapatite suspensions by slip casting", *J. Mater. Sci.*, **46**(15), pp. 5117-5128 (2011).
27. Freund, F. and Knobel, R.M. "Distribution of fluorine in hydroxyapatite studied by infrared spectroscopy", *Journal of the Chemical Society, Dalton Transactions*, **11**, pp. 1136-1140 (1977).
28. Golden, D. and Ming, D. "Nutrient-substituted hydroxyapatites: Synthesis and characterization", *Soil Sci. Soc. Am. J.*, **63**(3), pp. 657-664 (1999).
29. Lafon, J., Champion, E. and Bernache-Assollant, D. "Processing of AB-type carbonated hydroxyapatite Ca10-x(PO4)6-x(CO3)x(OH)2-x-2y(CO3)y ceramics with controlled composition", *Journal of the European Ceramic Society*, **28**(1), pp. 139-147 (2008).

30. Kim, H., Himeno, T., Kokubo, T. and Nakamura, T. "Process and kinetics of bonelike apatite formation on sintered hydroxyapatite in a simulated body fluid", *Biomaterials*, **26**(21), pp. 4366-4373 (2005).

31. Cai, Y., Zhang, S., Zeng, X., Wang, Y., Qian, M. and Weng, W. "Improvement of bioactivity with magnesium and fluorine ions incorporated hydroxyapatite coatings via sol-gel deposition on Ti6Al4V alloys", *Thin Solid Films*, **517**(17), pp. 5347-5351 (2009).

32. Van Loveren, C. "The antimicrobial action of fluoride and its role in caries inhibition", *J. Dent. Res.*, **69**, Spec. No: 676-81; discussion 682-3 (1990).

33. Marquis, R.E. "Antimicrobial actions of fluoride for oral bacteria", *Can. J. Microbiol.*, **41**(11), pp. 955-964 (1995).

34. Hong, I. and Koo, C.H. "Antibacterial properties, corrosion resistance and mechanical properties of cu-modified SUS 304 stainless steel", *Materials Science and Engineering: A*, **393**(1), pp. 213-222 (2005).

35. Dan, Z., Ni, H., Xu, B., Xiong, J. and Xiong, P. "Microstructure and antibacterial properties of AISI 420 stainless steel implanted by copper ions", *Thin Solid Films*, **492**(1), pp. 93-100 (2005).

36. Otsuki, S., Morshed, S.R., Chowdhury, S.A., Takayama, F., Satoh, T., Hashimoto, K., Sugiyama, K., Amano, O., Yasui, T., Yokote, Y., Akahane, K. and Sakagami, H. "Possible link between glycolysis and apoptosis induced by sodium fluoride", *J. Dent. Res.*, **84**(10), pp. 919-923 (2005).

Biographies

Raheleh Nikonam Mofrad received her master and bachelor degrees in Materials Science and Engineering from Sharif University of Technology and Ferdowsi University of Mashhad in 2012 and 2010, respectively. In 2014, she joined the Mechanical, Industrial and Aerospace Engineering Department at Concordia University in Canada to conduct a research on fabrication and characterization of porous silicon nitride ceramics with filtration applications.

Sayed Khatiboleslam Sadrnezhaad is a distinguished Professor at the Department of Materials Science and Engineering of Sharif University of Technology. His current interest is in the emerging bio-nano fields of the materials science and engineering discipline. His PhD dates back to 1979 from the Massachusetts Institute of Technology. So far, he has authored and coauthored five books, more than 600 technical papers and more than 60 patents.

Jalil Vahdati Khaki is a Professor at the Department of Materials Engineering, Faculty of Engineering of Ferdowsi University of Mashhad. His fields of study and research include mechanical alloying, thermodynamics and kinetics of materials, materials processing and extractive metallurgy. He is the editor-in-chief of Journal of Metallurgical and Materials Engineering which is published by Ferdowsi University of Mashhad. Dr. Vahdati has authored 140 journal and conference papers.